Daniel Øvstedal Fakhri

Sonochemical synthesis of Cu-Pt core-shell nanoparticles on a carbon support

Master's thesis in Chemical engineering and biotechnology
Supervisor: Frode Seland
Co-supervisor: Henrik Erring Hansen

October 2022

◨ NTNU
Norwegian University of
Science and Technology

Daniel Øvstedal Fakhri

Sonochemical synthesis of Cu-Pt core-shell nanoparticles on a carbon support

Master's thesis in Chemical engineering and biotechnology
Supervisor: Frode Seland
Co-supervisor: Henrik Erring Hansen
October 2022

Norwegian University of Science and Technology
Faculty of Natural Sciences
Department of Materials Science and Engineering

NTNU
Norwegian University of
Science and Technology

Preface

The work herein represents the culmination of my studies at the Department of Materials Science and Engineering at the Norwegian University of Science and Technology, NTNU, and is done for the degree Master of Science (MSc).

I would like to thank my PhD supervisor Henrik E. Hansen, for his enthusiasm towards the subject matter, insightful discussions and productive feedback. I would also like to thank my supervisor Frode Seland for all his help, guidance and patience. Finally, a large thanks to my family for all their love and support.

Abstract

Cu@Pt core-shell nanoparticles were synthesized by sonochemical reduction of $CuSO_4 \cdot 5\,H_2O$ in an aqueous buffer solution with a pH of 5 containing 9.9 mmol dm^{-3} formic acid, HCOOH, and sodium formate, NaCOOH, acting as a radical scavenger. The presence of Cu nanoparticles in the reaction solution were confirmed with UV-visible spectroscopy by the presence of a plasmon resonance peak at around 600 nm, visible as a shoulder in the obtained spectrum. Presence of Cu, as well as Cu_2O, in the extracted product was also confirmed by X-ray diffraction. The formation of Cu@Pt core-shell nanoparticles after addition of $PtCl_4$ to the reaction solution by galvanic replacement is further supported by the rapid decline of absorption observed with UV-Visible spectroscopy. Scanning (Tunneling) Electron Microscopy (S(T)EM) and Energy Dispersive X-ray Spectroscopy (EDX) images also support a core-shell structure by the co-location of Cu and Pt, and cyclic voltammograms confirm the presence of Pt at the surface. For a catalyst made from synthesized Cu@Pt core-shell particles supported on *carbon black* (Vulcan XC-72), linear sweep voltammetric measurements give an overpotential at -10 mA cm^{-2} of 34.8 mV $\pm$ 14.3 mV (90% confidence interval, T-distribution with $\nu = 2$).

Sammendrag

Cu@Pt kjerne-skall partikler ble syntetisert ved sonokjemisk reduksjon av $CuSO_4 \cdot 5H_2O$ i en vandig bufferløsning med pH 5 bestående av 9.9 mmol dm^{-3} metansyre, HCOOH, og natriumformat, NaCOOH, som valgt radikalsamler. Tilstedeværelse av Cu i reaksjonsløsningen ble bekreftet av en plasmon-resonanstopp rundt 600 nm med absorpsjonspektroskopi ved ultrafiolette og synlige bølgelengder, observert som en skulder i spektrumet. Tilstedeværelse av Cu og Cu_2O i produktpartiklene ble også bekreftet ved røntgendiffraksjon. Dannelsen av Cu@Pt kjerne-skall partikler etter tilsats av $PtCl_4$ til reaksjonsløsningen, ved en galvanisk erstatningsreaksjon, ble også støttet av den skarpt nedtagende absorbansen observert med UV-synlig spektroskopi. Elektronmikroskopi og energi-dispersive X-ray - bilder støtter også hypotesen om dannelse av kjerne-skall partikler, ettersom Cu og Pt er tilstede på samme områder i bildene. Syklisk voltammetri bekrefter videre at Pt er tilstede på overflaten av produktpartiklene. For en katalysator laget av de sonokjemisk syntetiserte Cu@Pt kjerne-skall partiklene heftet ved en karbon (Vulcan XC-72) - katalysatorstøtte ble overpotensialet ved -10 mA cm^{-2} målt til 34.8 mV $\pm$ 14.3 mV (90% konfidensintervall, T-fordeling med $\nu = 2$) ved lineær voltammetri.

Contents

1 Introduction

1.1 Background and motivation

One of the big problems of our time is climate change caused by the byproducts of the technologies that make up our modern world. A possible solution to this problem is a transition to more environmentally friendly technologies across many sectors; an important one being energy and transport. In these sectors, carbon-containing fuel sources, like coal, petrol or natural gas, are burned for energy. The challenge is thus to replace the fuel for something that doesn't contain carbon. A viable candidate is hydrogen, H_2, as it can be combined with oxygen, O_2, releasing energy and only water as a byproduct. This can be performed in a fuel cell to produce electricity directly, which is attractive for the transport industry, but it can also be included in fuel mixtures to replace some or all of the natural gas burned to drive turbines in power plants [1, 2].

Even though hydrogen does not release any harmful byproducts when it is used for energy, there are challenges associated with both its storage and production. Its specific energy ($J\,kg^{-1}$) is high, but its energy density ($J\,m^{-3}$) is quite low [3, Ch. 8]. This necessitates significant compression of the gas (and subsequent storage at high pressures), or significant cooling to cause liquefaction (and subsequent storage at cryogenic temperatures). Both of these operations require significant energy to perform [4]. On the production side, one way to obtain hydrogen is to split water into hydrogen and oxygen using electricity in a process called *electrolysis*. Electrolysis of water can be represented as

$$2\,H_2O\,(l) \xrightarrow{energy} 2\,H_2(g) + O_2(g) \tag{1}$$
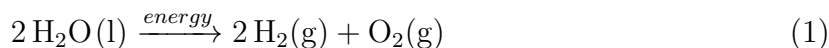
This is achieved by immersing two metallic conductors, called *electrodes*, in water and passing a current through the system. Either acidic or basic solutions can be used for this process. In an acidic solution, the electrode where H^+ ions are reduced is called the *cathode*, and the electrode reaction can be represented as

$$2\,H^+(aq) + 2\,e^- \longrightarrow H_2(g) \tag{2}$$

This reaction is called the *hydrogen evolution reaction* (HER). While it is fast in an acidic solution, it is slow in a basic solution because it has to be produced from water molecules instead of H^+.

$$2\,H_2O\,(l) + 2\,e^- \longrightarrow H_2(g) + 2\,OH^-(aq) \tag{3}$$

In both cases, the reaction taking place at the other electrode, the *anode*, is the *oxygen evolution reaction* (OER), which is an inherently very slow reaction.

$$2\,H_2O\,(l) \longrightarrow O_2(g) + 4\,H^+(aq) + 4\,e^- \tag{4}$$
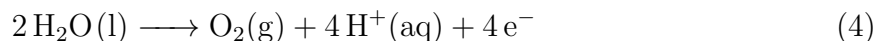
Due to its inherent slowness, one is forced to apply a higher voltage to the system than that which is required by thermodynamics. This increase in voltage is called an *overpotential* and is directly related to the energy lost in the process. The overpotential can be significantly reduced by using different electrode materials, and the study of how to achieve this is called catalysis, or specifically electrocatalysis for reactions involving electrodes. As the use of an efficient electrocatalyst can greatly reduce the energy required to run the reaction, it is often the crux of the entire process of hydrogen production.

Among the possible elements and compounds available to catalyse the HER, Pt is one of the best performing. However, being a noble metal with low occurence in the earth's crust it is prohibitively expensive to use in large quantites. Significant effort has therefore gone into finding ways to lessen the amount used for a catalyst, or to remove the need for Pt altogether by using other materials [5]. One of these avenues of investigation has been into so-called core-shell nanoparticles; nanoscale spheres consisting of one material as the inner core and another forming the outer shell, commonly denoted core@shell, e.g. Cu@Pt for a core-shell particle with an inner Cu core and a Pt shell. Such particles can lessen the amount of Pt required, as the inner shell may consist of a much cheaper metal, but also change the electronic structure of the shell compound, potentially also achieving greater catalytic activity.

Numerous chemical synthesis methods exist to produce core-shell nanoparticles, however these commonly involve the use of different surfactants and reduction agents which can be expensive and may introduce more complexity into the chemical process by requiring extra separation steps after the desired product has been produced. It would therefore be interesting if there was a way to produce these nanoparticles without using complicating reagents. *Sonochemistry*, which is the application of ultrasound to perform chemistry, offers just such an alternative. When water is subjected to ultrasound it is split into highly reactive radicals which can be used to perform different reactions. It is the subject of this master's thesis to investigate whether a sonochemical method can be used to produce core-shell nanoparticles and overcome some of the challenges mentioned above.

1.2   Aim and scope of the work

In the literature, Cu, Pt and Cu@Pt core-shell nanoparticles have been produced by a variety of methods [6, 7, 8, 9, 10]. Sonochemical methods have also been emplyed to create monometallic nanoparticles of noble metals [11, 12, 13, 14]. The aim of this master's thesis is to continue a previous investigation where Pt nanoparticles on a C support were synthesized sonochemically using ethanol as a radical scavenger [15]. Here, Cu@Pt core-shell nanoparticles will be synthesized sonochemically and its performance as a catalyst for HER will be evaluated.

To achieve this goal, the sonochemical synthesis will be performed with formate, $HOOC^-$, as the radical scavenger and evaluated by UV-visible spectroscopy. The nature of the synthesized product will be investigated by X-ray diffraction spectroscopy (XRD), scanning (Tunneling) electron microscopy (S(T)EM), energy dispersive X-ray spectroscopy (EDS) and cyclic voltammetry (CV). Finally, the performance of the product as a catalyst will be evaluated by linear sweep voltammetry (LSV).

2 Theory

As the work in this master's thesis is a continuation of the project thesis dealing with the same subject matter, much of the theory in [15] has been reused here, with some changes and additions. Section 2.3 on absorption spectroscopy remains largely unchanged except for the omission of Weissler dosimetry, but an additional section on the optical properties of Cu nanoparticles in aqueous solution has been added.

2.1 Sonochemistry

When a liquid medium is subjected to ultrasound, a pressure wave travels through the liquid causing cycles of alternating compression (becoming denser) and rarefaction (becoming less dense) [16, p. 2-5]. The negative pressure during rarefaction creates a pulling effect which can cause cavities to form in the liquid. In practice, these are always gas cavities, or bubbles. Once such a bubble is formed, it oscillates between compression and expansion according to the applied acoustic frequency. The net effect is that the bubble grows over time until it reaches its resonance size, where the bubble oscillation frequency approaches that of the driving frequency. As the oscillation amplitude then increases without bound, the bubble eventually implodes causing the centre of collapse to reach temperatures of around 5000 K and pressures of around 500 atm [16, p. 6-9, 21]. This is hot enough to cause pyrolysis of the solvent; it decomposes via homolysis of its bonds, forming radicals. When this is induced by ultrasound, it is called *sonolysis*. During sonolysis, there are three distinct regions in the microbubbles formed that are important for chemical reactions, as indicated in Figure 2.1. Region (i) was already mentioned, where the high temperature and pressure generates radicals from both volatile solutes and gases that have diffused into the bubble during the expansion phase [16, p. 9]. In the case of an aqueous solution, water decomposes into hydrogen ($H \cdot$) and hydroxyl ($HO \cdot$) radicals, called *primary radicals*, which can be represented by the following reaction equation,

$$H_2O \xrightarrow{\text{)))}} H \cdot + HO \cdot \tag{5}$$

where))) indicates sonication. These radicals can react with each other to form H_2, H_2O_2 or back to H_2O. If other compounds are present in the bubble, radicals of these are readily formed and reactions between the different species, as well as recombination of different radicals, also occur. In the case of $O_2(g)$, oxygen radicals and ozone are among the compounds formed [16, p. 10][17]. It has been shown that bubble temperatures during collapse are higher with Ar gas dissolved in solution than with O_2 [18]. Ar, being a monoatomic noble gas, cannot dissociate into radicals of its own, making it a common saturation gas in sonochemistry.
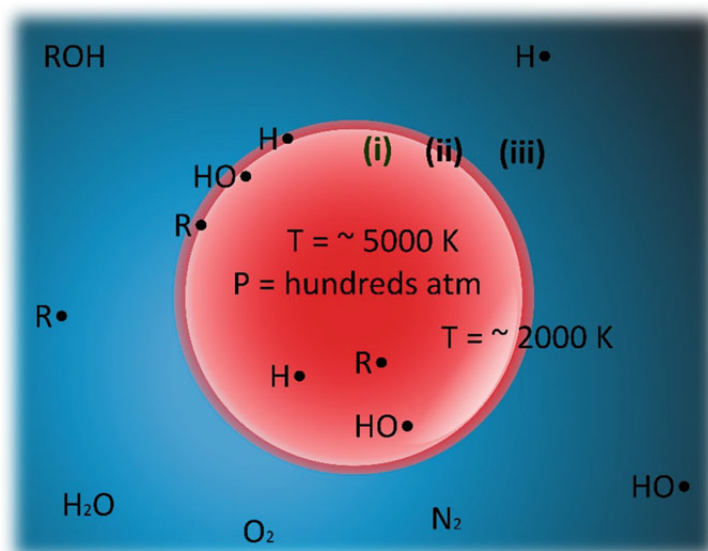
Figure 2.1: Illustration of sonochemical reactions sites on a microbubble during sonolysis. (i) Inner cavitation bubble, (ii) shell of the microbubble and (iii) bulk solution. Source: [16, p. 8].

Region (ii) is the interface between the bulk solution and the bubble, which can reach temperatures of up to 2000 K during bubble collapse. If surface active molecules like alcohols or other surfactants are present, *secondary radicals* are formed from these by reaction with the primary radicals. These are also called *radical scavengers*. Radicals can also be formed by pyrolysis of the surfactants in the interfacial region [19].

Region (iii) is the bulk solution, in which solutes that are not surface active remain [16, p. 10]. These may react with the radicals which have managed to escape the cavitation bubbles. One commonly used bulk radical scavenger is sodium formate, HCOONa. Having only one carbon atom it will always give up its α-hydrogen atom and form the highly reducing $\cdot CO_2^-$ radical ($E^0 = -1.9\,\mathrm{V}$) [20].

$$\cdot OH + HCOO^- \longrightarrow \cdot CO_2^- + H_2O \qquad (6)$$
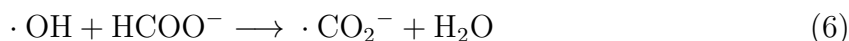
It is well established that noble metal nanoparticles can be produced by interaction with reducing radicals [21, 12, 14, 13]. There are proposed three different mechanisms for such reduction of noble metal cations in solution [19, 12, 13]:

1. Direct reduction by hydrogen primary radicals.

2. Reduction by secondary radicals formed from scavenging of primary radicals.

3. Reduction by secondary radicals formed by pyrolysis of the surface active species in the interfacial region during cavitation events.

In either case, a schematic representation of the reduction of a metal cation in solution can be given as [21]:

$$\mathrm{M}^{n+} + \text{reducing species}(\mathrm{R}\cdot,\mathrm{H}\cdot,\text{etc}\cdot) \longrightarrow \mathrm{M}^0 \qquad (7)$$

2.2 Catalysis

A catalyst a chemical compound that changes the rate of a chemical reaction while remaining unchanged itself. It does this by allowing the reaction to proceed by a different reaction pathway than that which would have been available without the catalyst. The new pathway has a lower Gibbs energy of activation, which is the largest free energy difference between the reactants and any intermediates formed during the reaction. *Heterogeneous* catalysis means that the catalyst is present in a phase different from the reactants. Commonly, the catalyst is a solid and the reactants are in the liquid or gas phase. Catalyzing electrochemical reactions occurring at an electrode interface is called electrocatalysis. In these cases the reactions take place in the fluid-solid interface, so a larger surface area is correlated to a higher reaction rate. A surface area that is much larger than the linear dimensions of the catalyst sample can be achieved by using compounds with a rough or porous structure. [22, Ch. 10], [23, Ch. 26]

A compound with a specific catalytic property may be dispersed onto another less active compound with a high surface area to create a good catalyst. In this case the less active compound is referred to as the *support*. Pt nanoparticles deposited on a porous carbon support is an example of such a catalyst. For heterogeneous catalytic reactions to occur, one or more of the reactants have to become attached to the surface. This process is called *adsorption* and can occur in one of two ways; *physisorption* or *chemisorption*. Physisorption, or simply physical adsorption, is similar to the condensation of a gas on a surface. It is an exothermic process with a relatively small heat of adsorption (on the order of 10 kcal mol^{-1}). For chemisorption, surface-adsorbate bonds are formed which changes the chemical reactivity of the adsorbate. An example is the dissociative chemisorption of H_2 on Pt, where hydrogen molecules dissociate into hydrogen atoms bonded to Pt surface atoms. Sites where appreciable chemisorption occur are called *active sites* and they can be unsaturated atoms on a surface, but also other surface irregularities like dislocations, edges of crystals and cracks along grain boundaries [22, p. 650].

A final factor determining catalytic activity is how strongly the adsorbate is bound to the active site. If the bond is too weak, very little surface coverage of reactants is attained and the catalytic activity will be low. On the other hand, if the bond is too strong the adsorbate may not be able to react further or may be immobilized on the surface, also leading to low catalytic activity. Considering reaction rates as a function of adsorption enthalpy of the reactants, these facts lead to a so-called "volcano" behaviour, where a maximum in catalytic activity is usually found in a "sweet spot" between small and large adsorption enthalpies [24, p. 957]. In the case of metal particles at a surface, such chemisorption can be understood through the theory of Lewis acidity; the metal particles behave as Lewis acids, accepting electron density from the adsorbing species [23, Ch. 4, 26]. The determining factor of the adsorption enthalpy is really the matching of energy levels between the highest occupied molecular orbital (HOMO) of the adsorbate and the lowest unoccupied molecular orbital (LUMO) of the catalyst species [25]. These energy levels are determined by the molecular orbital overlap between the

atoms in the catalyst, and thus varying the elemental composition give different energy levels [23, Ch. 26]. It is therefore possible to create very efficient catalysts by nanoscale engineering of catalyst structures. Creating core-shell structures is a way to achieve this tuning of molecular orbital energy levels, while also saving costs for expensive elements [26]. This has been successfully demonstrated previously [8, 7, 27, 28]. Zhu et.al [8] performed a successful two-step polyol synthesis of Cu@Pt which demonstrated an improved ORR activity compared to Pt alone. A similar work was also done by Sarkar et.al [7] where a Cu@Pt core-shell catalyst was prepared in a two-step process where the Cu core was synthesized by chemical reduction and the Pt-shell was created through galvanic displacement. They also observed an increased activity towards ORR and attribute this to a modification of the electronic configuration of the outer Pt shell.

As seen in the work just discussed, *galvanic displacement* seems to be a commonly applied technique to achieve core-shell structures. A galvanic displacement reaction is a redox reaction between two elements with different reduction potentials where a solid with a lower reduction potential is oxidized and the ion in solution with the a positive reduction potential is reduced

$$N^{n+}(sol) + M(s) \longrightarrow N(s) + M^{n+}(sol) \tag{8}$$

At the face of it, this seems to be a simple way to replace the outer atoms of a particle with another more noble element.

2.3   UV/VIS-spectroscopy, dosimetry and characterization

The separation of energy levels of molecular orbitals are of an order of magnitude such that electron transitions between them can be studied by interaction with UV and visible wavelengths of light. In *absorption spectroscopy*, the *net* absorption of incident radiation is measured as the frequency is varied. It is the net absorption that is measured, because both absorption and emission are stimulated and the detector measures the difference [24, p. 476]. Chemical species in solution can have very distinct absorption spectra and this can therefore be used to identify the species present.

When a sample is exposed to radiation, it is found empirically that the transmitted intensity, I (W m^{-2}), is proportional to the incident intensity I_0 and varies with the length, L (cm), of the sample and the molar concentration of species i, c_i (mol dm^{-3}), according to what is known as the Beer-Lambert law [24, p. 479]:

$$I = I_0 10^{-\epsilon c_i L} \tag{9}$$

Where ϵ is the molar absorption, or "extinction", coefficient, commonly given in units of dm^3 mol^{-1} cm^{-1}. However, the intensity of light transmitted through a sample relative to the intensity of incident radiation is commonly reported as the *transmittance*, T:

$$T = \frac{I}{I_0} \tag{10}$$

and the *absorbance* is given as the logarithmic measure of its inverse

$$A = \log \frac{1}{T} \tag{11}$$

Given this, the commonly used version of the Beer-Lambert law is simply:

$$A = \epsilon c_i L \tag{12}$$

By *dosimetry* we mean the determination of the concentration of radical species in solution using certain chemical reagents and their spectroscopic measurement. Only dosimetry using $TiOSO_4$ as the reagent was used here.

$TiOSO_4$-dosimetry is based on the formation of a peroxotitanium (IV) complex from Ti(VI) and H_2O_2, which has a strong absorption peak at 411 nm [29, 30]. The molar absorption coefficient for this complex was measured in a separate calibration experiment with commercial H_2O_2 to be $\epsilon = 787$ dm^{3}mol^{-1}cm^{-1}. As two $HO\cdot$ radicals are needed to form H_2O_2, the concentration of $HO\cdot$ radicals can be estimated as $[HO\cdot] = 2[H_2O_2]$.

The concentration of Pt-ions in solutions can be measured by addition of KI, as it forms complexes with Pt(IV) and Pt(II); $PtI_6{}^{2-}$ and $PtI_4{}^{2-}$ respectively. These have distinct absorbance peaks in the visible spectrum at 495 nm ($\epsilon = 9400$ dm^{3}mol^{-1}cm^{-1}) and 388 nm ($\epsilon = 5500$ dm^{3}mol^{-1}cm^{-1}) respectively [21].

2.3.1 Optical properties of Cu nanoparticles in water

A plasmon is a quantized oscillation of the electron density in a metal [31, Ch. 14]. Such an oscillation can be produced by interaction of metal nanoparticles with light of an appropriate wavelength. The most notable feature in the absorbance spectrum of colloidal Cu-nanoparticles is the plasmon resonance peak between 400 nm to 600 nm. Calculations based on Mie theory for spherical particles with a diameter of 10 nm give a peak at around 580 nm [32], but there are significant variations found depending on the size of the particles and surfactants used [33]. UV-visible spectra of Cu nanoparticles in aqeueous solutions based on such varied synthesis methods have been obtained in numerous other works [34, 35, 36, 37, 38]. It is of interest here to have these references for the spectra of Cu nanoparticles to verify its presence during the sonochemical synthesis.
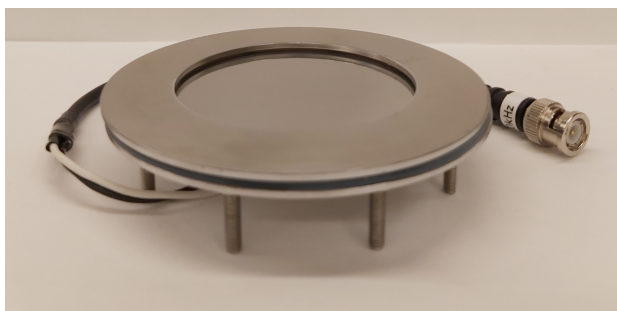
3 Experimental

3.1 Equipment and Assembly

The equipment and experimental setup used here is the same as in [15], and has been recounted here to elucidate the experimental work. The main experimental unit is a glass cell made at the NTNU Glassblowing workshop and a plate transducer made by *Honda electronics*, see Figure 3.1. The glass cell consists of an inner cylindrical region with an empty bottom where the reaction solution will be in contact with the plate transducer. There is also an outer annular region, separated from the inner region, with inlet and outlet ports for coolant to flow through. Additionally, the top of the cell has multiple necks for instrument access.

(a)

(b)

Figure 3.1: Experimental equipment; glass cell on the left (a), and plate transducer on the right (b).

The plate transducer used has a frequency of 346kHz. Due to a mismatch in impedance between the signal generator (50 Ω) and the plate transducer (213 Ω) an *impedance matcher*, model: T1K-7A, has been used as well. A signal generator was also used to power the plate transducer, model: AG1012. Both are produced by T&C power and shown in Figure 3.2.

Assembling the transducer and the glass cell is simple; pictures for a step-by-step procedure are shown in Appendix A. A silicon ring is first placed on the outer edge of the transducer, followed by the glass cell. Finally, a pair of plastic rings fastened with screws hold the assembly together.

Figure 3.2: Experimental equipment; signal generator AG1012 (a), and impedance matching unit (b).

A figure of the experimental setup during an active experiment is included below.
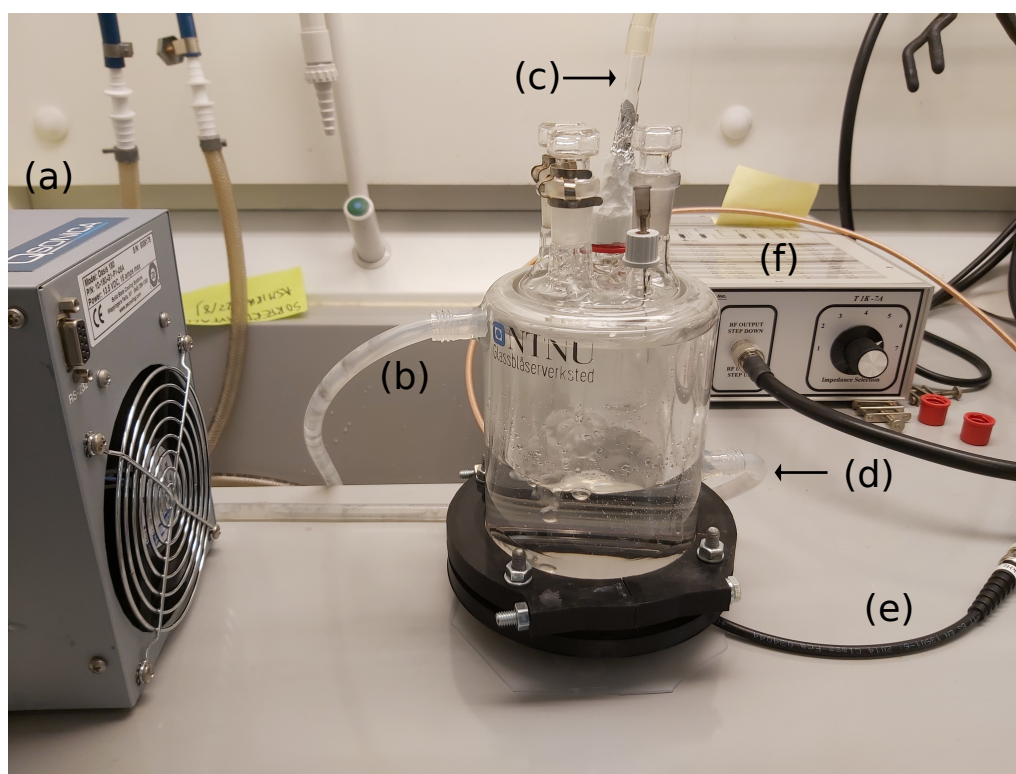

Figure 3.3: Picture of the setup for the sonochemical reactor during an experiment. (a) is the cooling unit, (b) is the reactor coolant inlet, (c) is the gas inlet, (d) is the coolant outlet and (e) is the transducer connector. The impedance matcher, (f), is also visible in the background.

3.2 Synthesis

All sonochemical synthesis was performed using the same sonicator plate with the signal generator set to a frequency of 346 kHz and a power of 50 W. The cooling system for the reactor was also set to 3°C for every experimental run. The sonochemical formation of $\cdot$OH radicals under these conditions has previously been estimated to be 12 μmol dm^{-3}

min^{-1} [21]. To give an overview of the synthesis procedure, an experimental flow chart is presented in Figure 3.4.
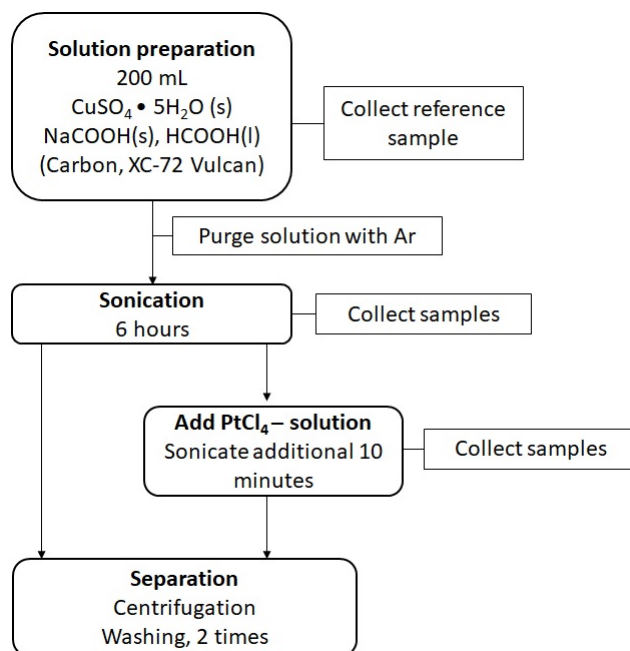

Figure 3.4: Experimental flow chart for the sonochemical synthesis.

3.2.1 Cu-synthesis

A 200 mL buffer solution with a pH of 5 containing 2 mmol dm^{-3} Cu^{2+}(aq) was prepared from CuSO$_4 \cdot 5$ H$_2$O(s), HCOONa(s) and concentrated ($\geq$ 98 %) HCOOH(l), giving a concentration of 9.908 mmol dm^{-3} HCOOH(aq). This solution will henceforth be referred to as the *copper buffer solution*. It was then added to the reactor and bubbled with Argon gas for 20 minutes to make sure that no dissolved oxygen was present, while the cooling system was set to 3°C and kept at this temperature throughout the experiment. Sonication was then initiated, lasting 360 minutes, with samples taken throughout for characterization by ultraviolet-visible spectroscopy. No reagent was added to these samples, but on separate experiments a 0.45 μm filter was used to remove the contribution of the nanoparticles.

After sonication was complete, the solution was centrifuged to separate the product particles. Following separation, the product was further washed in a 50/50 by volume water/ethanol (96 %) mixture and centrifuged an additional 2 times to remove any impurities and residual solvent that may have adsorbed onto the particles.

3.2.2 Cu-Pt synthesis

The copper buffer solution was prepared and experimental parameters were set as in the pure Cu-synthesis. Additionally, a 50 mL solution containing 0.2 mmol dm^{-3} PtCl$_4$(aq) was prepared. The copper buffer solution was sonicated for 360 minutes, after which the PtCl$_4$ was added and sonication continued for another hour giving a total reaction

time of 420 minutes. Preliminary results indicating fast reduction of Pt^{4+}(aq) led to a reduction of the additional sonication time to 10 minutes, for a total reaction time of 370 minutes. Samples were taken throughout and excess KI(aq) were added to those taken after addition of $PtCl_4$(aq), to monitor the concentration of Pt^{4+}/Pt^{2+}.

Separation and washing of the reaction product was done as for the pure Cu-synthesis.

3.2.3 Cu-Pt and C synthesis

The sonochemical synthesis already detailed was also performed with 27.11 mg of Carbon Black - Vulcan XC-72, added to the copper buffer solution at the start of the synthesis, giving a metal/C support ratio of 20 % by weight. Experimental parameters and sonication duration was kept the same, and separation and washing was performed identically.

3.2.4 Chemical reduction synthesis

The copper buffer solution was prepared in a large beaker open to air. While stirring, an excess of $NaBH_4$(s), giving a molar ratio of BH_4^- to Cu^{2+} of 5:1, was quickly added all at once and samples were collected for UV-visible measurements.

3.3 Characterization

3.3.1 UV/VIS Spectroscopy

All samples taken during sonochemical synthesis were transferred to a cuvette and characterized by UV-visible spectroscopy using a *Thermo scientific evolution* 220 spectrophotometer. The wavelength range was set to 200 nm to 900 nm with a resolution of 1 nm and a scanrate of 100 nm min^{-1}.

3.3.2 XRD

Sonochemically synthesized nanoparticles were dispersed in a 96% ethanol solution by immersing the sample in an ultrasound bath for 10 minutes. The solution was then drop-cast onto a "Si-flat insert" disk and the solvent was allowed to evaporate before it was covered with kapton® polyimide film. The X-ray instrument used was a Bruker D8 ADVANCE DaVinci with $CuK\alpha$ radiation. The data was gathered on a low-crystalline program taking 60 minutes at an angular range of $[15°, 75°]$ with a resolution of $0.3°$.

3.3.3 Electron microscopy

Scanning tunneling electron microscope imaging (STEM) and energy dispersive X-ray spectroscopy (EDX) was performed with a Hitachi High-Tech SU9000 electron microscope at NTNU Nanolab. All investigated samples were prepared by dispersing the product particles from the sonochemical synthesis in a 96 % ethanol solution and immersing the solution in an ultrasound bath until satisfactory mixing was achieved. This solution was then drop-cast onto a Caspilar Carbon/Gold TEM-grid, and allowed to evaporate.

3.3.4 Electrochemical characterization

An electrode ink was prepared by mixing 10 mg of product particles from the "Cu-Pt and C" synthesis with 475 µL H_2O, 475 µL isopropanol and 50 µL nafion (5 wt%) and then dispersing the solution by subjection to an ultrasound bath for 10 minutes. This solution was spin-cast onto a glassy carbon electrode with a geometric surface area of 0.196 cm^{-2}. The electrode was cleaned and polished beforehand using solutions with different sized alumina particles (0.05 µm to 0.5 µm). This formed the working electrode and a graphite rod was used as the counter electrode.

All electrochemical measurements were performed using an Ivium n-stat potentiostat in a 0.5 M H_2SO_4(aq) electrolyte using a reference hydrogen electrode (RHE). The solution was bubbled with Ar(g) for approximately 10 minutes to remove any dissolved oxygen, and the gas was supplied just above the solution during measurement to maintain an Ar-atmosphere.

Cyclic voltammetry (CV) was first performed to stabilize the catalyst. We performed 25 total cycles at a voltage range of 0.07 V to 1.5 V with steps of 1 mV and a scan rate of 50 mV s^{-1}. Linear sweep voltammetry was then performed in the HER potential region, from 50 mV to -50 mV and -100 mV at steps of 1 mV and a scan rate of 1 mV s^{-1}, where IR-compensation was taken into account after measurements were performed. A compensation resistance of 4.7 Ω was obtained from electrochemical impedance spectroscopy at 1 kHz using the same experimental conditions as described above.

4 Results

4.1 UV-visible spectroscopy

The results from UV-visible spectroscopy of the synthesis procedure are presented in Figure 4.1 below. Figure 4.1a shows the spectra taken during sonochemical synthesis of Cu. Notice the increase in absorbance with time and the formation of the shoulder at around 600 nm after 6 h. Before sonication (0 h) a peak belonging to Cu^{2+} can be observed between 700 nm and 800 nm. A spectrum from the same synthesis where the sample has been filtered is presented in Figure 4.1b. Notice the decreasing absorbance with time, indicating a decrease in Cu^{2+}. Figure 4.1c is the spectra obtained during the Cu-Pt synthesis, taken after addition of $PtCl_4$, where KI was added after extraction of the sample. Note the sharp decline in absorbance after only a minute, followed by no observable change to the absorbance peak of Pt^{4+}. Finally, Figure 4.1d shows the spectra taken from a chemical reduction synthesis of Cu^{2+} using $NaBH_4$. As time increases, the absorbance decreases and the peaks become redshifted and less sharp.
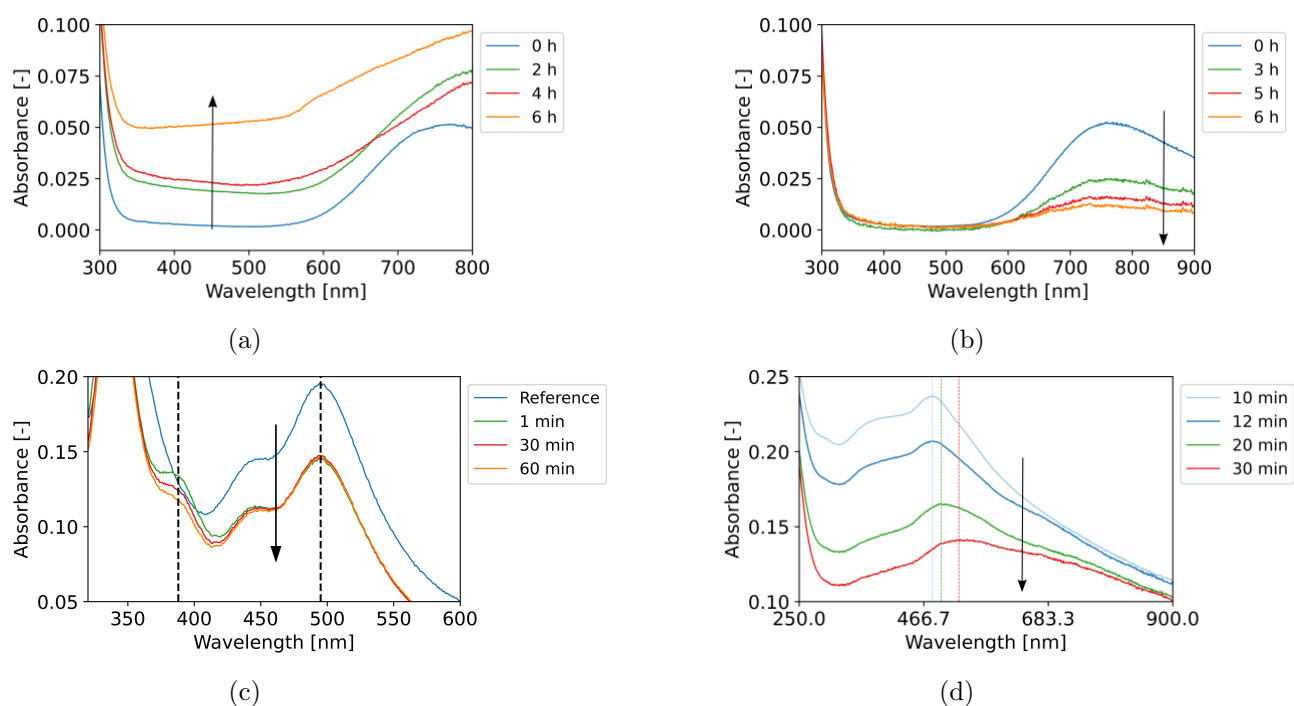

Figure 4.1: UV/visible spectra. Figures (a) and (b) are samples from the Cu synthesis taken during the first 6 hours, with and without filtering respectively. Figure (c) shows the development of Pt^{4+}/Pt^{2+}, where the dashed vertical lines at 495 nm and 388 nm are the absorbance peaks of the $PtI_6{}^{2-}$ and $PtI_4{}^{2-}$ - complexes, respectively. Figure (d) are samples taken during the chemical reduction of Cu^{2+} using $NaBH_4$, with dashed vertical lines indicating absorbance maxima.

4.2   X-ray diffraction

X-ray diffractograms from the product particles of the Cu and Cu-Pt syntheses are presented in Figure 4.2a. Spectrum (1) belong to product particles taken from the Cu synthesis, whereas spectrum (2) are taken from product particles obtained from the Cu-Pt synthesis. Diffraction peaks belonging to metallic Cu can be observed at 43.3° (111), 50.4° (200), and 74.0° (220), whereas those belonging to cubic Cu_2O can be found at 2θ angles of 29.5° (110), 36.3° (111), 42.2° (200), 61.1° (220), and 73.2° (311). The two peaks between 20°- 28° belong to the kapton™film used to cover the sample [39]. Note the absence of metallic Cu peaks in (1) and their appearance in (2). For comparison, simulated X-ray diffractograms for Cu and Cu_2O are included in Figure 4.2b obtained from *materialsproject.org* [40, 41]. Metallic fcc Pt would have had peaks at 39.2° (111), 45.6° (200), and 66.5° (220) but these cannot be observed.
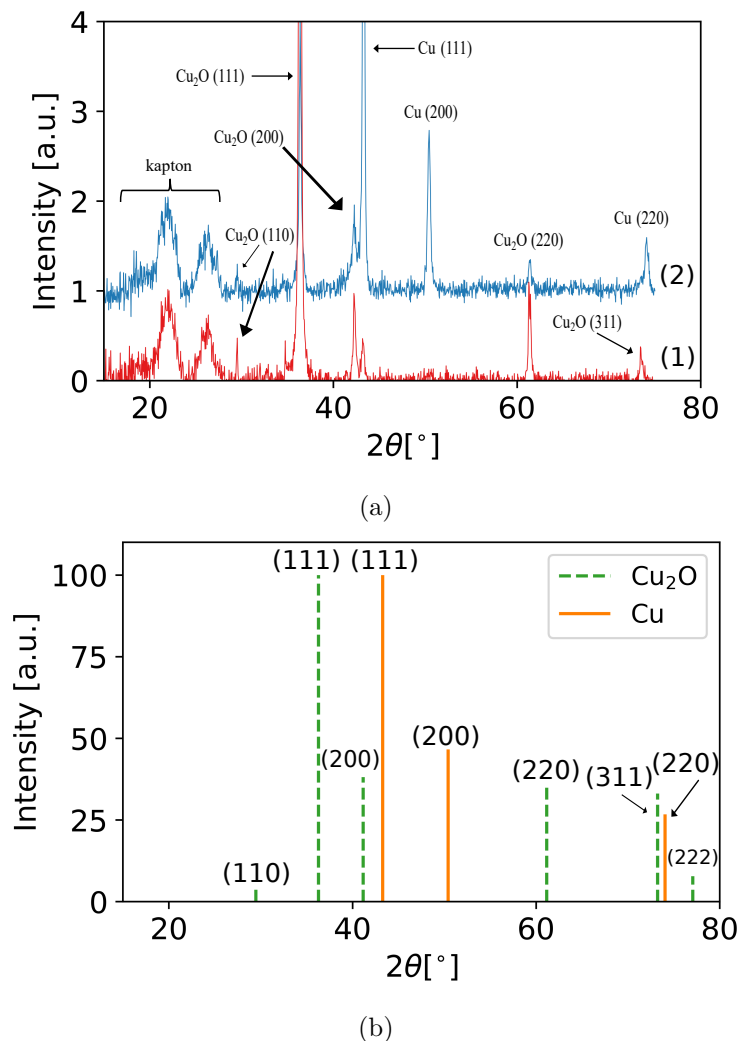

(a)

(b)

Figure 4.2: X-ray diffraction spectra. (a) shows experimental spectra, whereas (b) shows simulated spectra. In (a), (1) is from the product obtained from the Cu synthesis and (2) is from the product of the Cu-Pt synthesis.

14

4.3 STEM and EDX

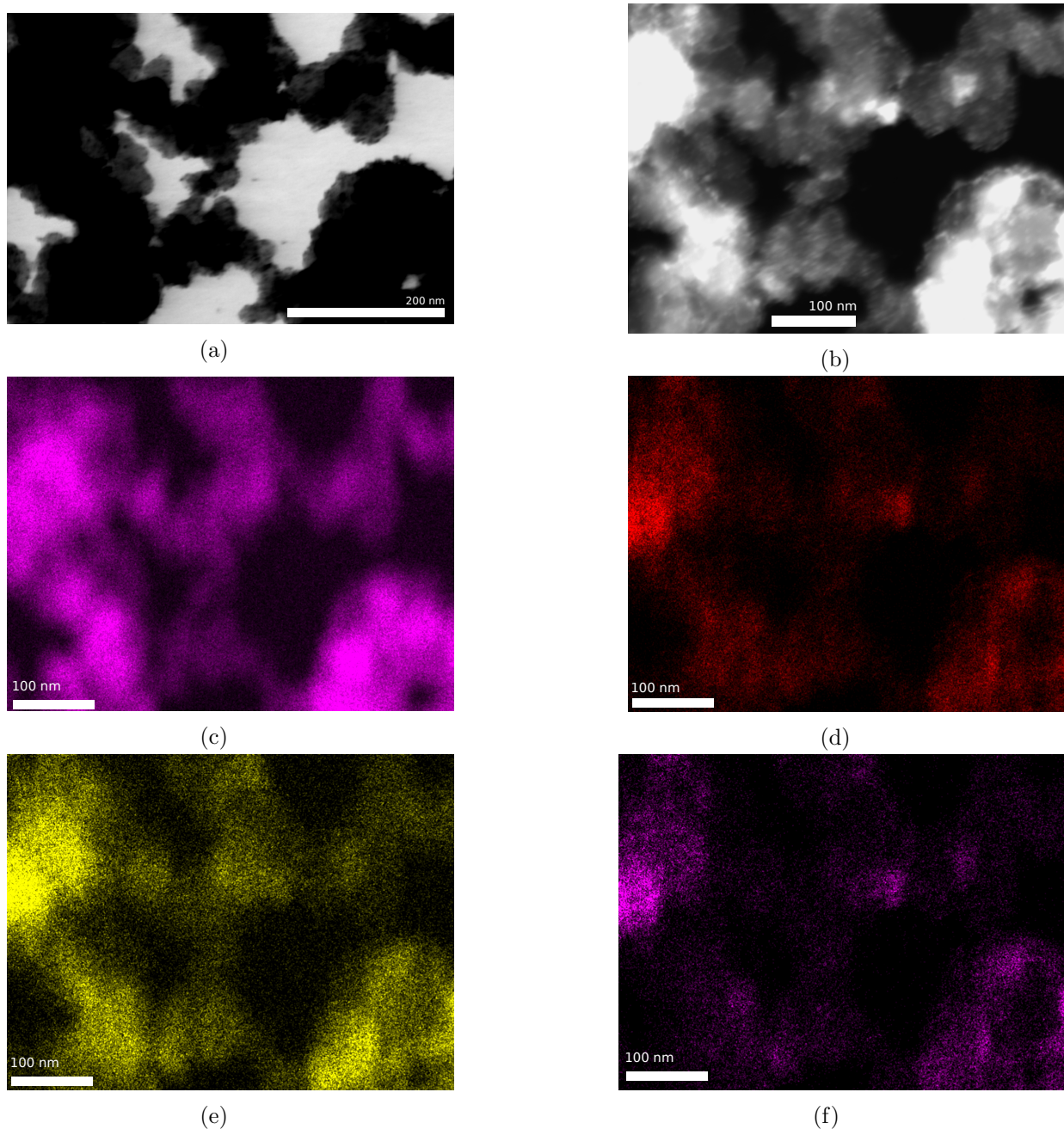

Figure 4.3: S(T)EM images captured of sonochemically synthesized Cu@Pt on C support samples aquired in bright field mode (a) and secondary electron mode (b), along with EDX map scans of carbon (c) copper (d) oxygen (e) and platinum (f).

The EDX maps in Figure 4.3d and Figure 4.3f show that the signal from Cu and Pt are overlapping. This also coincides with the bright parts observed in the secondary electron image in Figure 4.3b. C and O are also present over the entire sample as indicated by Figure 4.3c and Figure 4.3e. Careful examination of Figure 4.3a reveals the presence of

small dark spots on the thinner parts of the carbon support.

4.4 Electrochemical characterization

Cyclic voltammograms of the prepared catalyst electrode are shown in Figure 4.4. The first cycle in a series of voltammograms was chosen for the Cu on C support sample, curve (2), as we wanted to investigate whether a peak after 0.34 V would appear, indicating oxidation of metallic Cu. Observe that no such peak is present. The first and last cycle are given in Appendix B. The distinct characteristics of Pt are clearly visible in curve (1), which are mirrored by the Cu@Pt sample in curve (3). Notice also the reduced current density in curve (3) compared to curve (2).
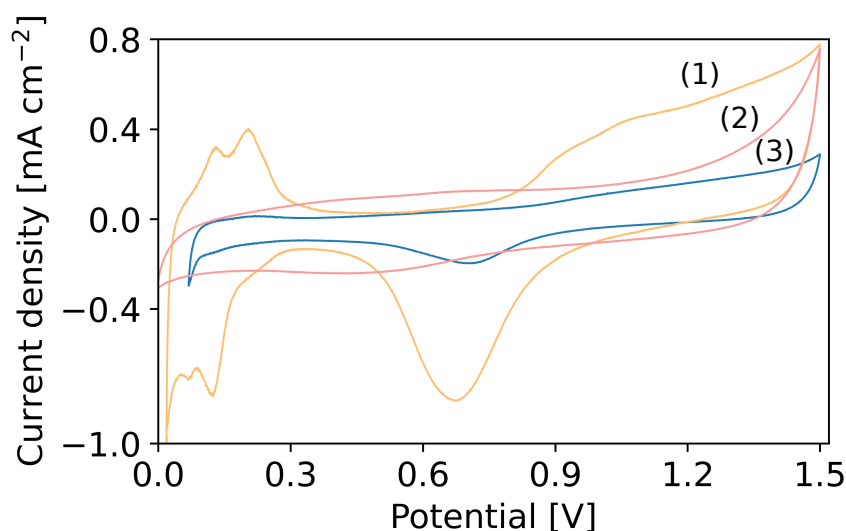

Figure 4.4: Cyclic voltammogram of sonochemically synthesized nanoparticles on C support. The numbers refer to the curve directly underneath them. (1) is Pt on C, (2) is Cu on C and (3) is Cu@Pt on C. (1) and (2) were taken from previous work [15].

Linear sweep measurements in the hydrogen evolution region are presented in Figure 4.5. Figure 4.5a shows the current density normalized for geometric surface area, giving an overpotential of the Cu@Pt sample at -10 mA cm^{-2} of 34.8 mV $\pm$ 14.3 mV (90% CI, T-distribution with ν=2). For the Pt samples, the overpotential at -10 mA cm^{-2} was found to be 29.0 mV and the Cu on C sample did not exhibit any significant hydrogen evolution. Figure 4.5b shows the current density normalized for the mass of Pt. Notice that the Cu@Pt sample then has a higher mass activity compared to the pure Pt on C sample.
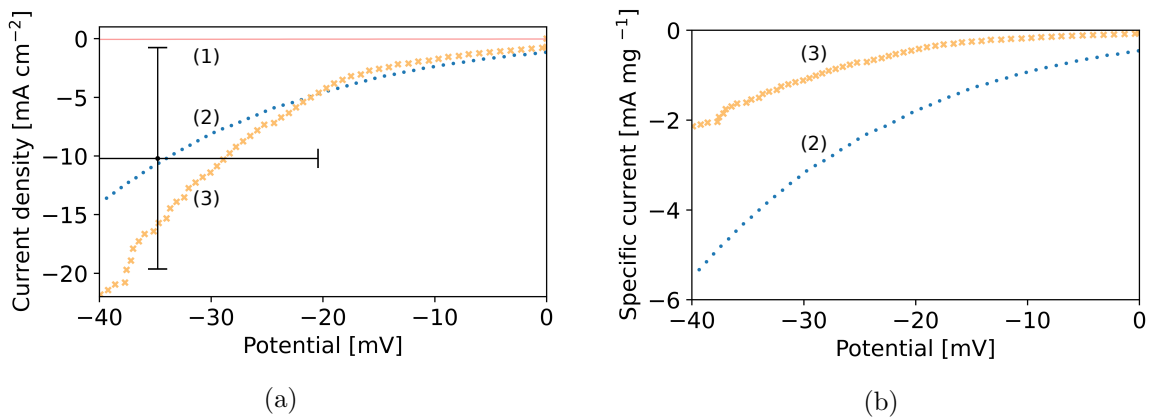
Figure 4.5: Linear sweep voltammetric measurements of three different samples of sonochemically synthesized nanoparticles supported on Carbon XC-72 in the hydrogen evolution voltage region, using a 0.5 mol dm^{-3} H$_2$SO$_4$ electrolyte and RHE. Figure (a) shows the current density normalized for the geometric electrode area. Figure (b) shows the current normalized for the weight of Pt used in the catalyst in milligrams. In (a), curve (1) is Cu on C, curve (2) is Cu@Pt on C and curve (3) is Pt on C. The same holds for (b). Curve (2) is an average of three measurement series done on the sample, see Appendix B.

5   Discussion

We believe that we have managed to synthesize Cu@Pt core-shell nanoparticles. This is supported in part by the X-ray diffractograms Figure 4.2, which show the presence of metallic Cu only after the addition of $PtCl_4$. This is assumed to be due to the formation of a protective layer of Pt formed by galvanic displacement during the synthesis, preventing the oxidation of Cu. The CV of the Cu@Pt-sample in Figure 4.4 supports that this protective layer consists of Pt. In addition, the LSV in Figure 4.5 clearly shows that the Cu-Pt and Pt-samples have affinity for the HER and demonstrate a significant increase in Pt mass activity for the Cu-Pt sample, whereas no response can be observed for the Cu samples. Finally, the EDX maps in Figure 4.3 further support a core-shell structure by showing the overlap between Cu and Pt. In summary, all the results support the hypothesis of a core-shell structure having been achieved.

The X-ray diffractograms in Figure 4.2 do not exhibit any evidence of metallic Cu in the samples from sonochemical syntheses without Pt. We believe metallic Cu is formed during sonication, but that an oxidation occurs upon drying the product in air. That metallic Cu does indeed form during the sonochemical synthesis is supported by the emerging shoulder at around 600 nm in Figure 4.1a, which coincides with the Cu plasmon peak discussed in section 2.3.1. In Figure 4.1b we also observe a decrease in the absorption peak observed in the reference sample with time, which is attributed to the decrease in concentration of Cu^{2+}. The oxidation of Cu is supported by the absorbance spectrum from the chemical synthesis shown in Figure 4.1d, which was performed open to air; it can be inferred from the decrease in magnitude and redshifting of the absorbance peak at 482 nm with time. The conjecture of the formation of a protective Pt shell by galvanic replacement is supported by Figure 4.1c, where a sharp decrease in the absorbance peak of Pt^{4+} is observed after a minute, followed by no observable change for the next hour. If the reduction of Pt occurs by galvanic displacement, we would expect Pt to react quickly with the available Cu and then plateau, which is consistent with the UV-visible spectra. Thus, when the product is dried in air oxidation is prevented due to the Pt layer, which is supported by the emergence of the metallic Cu reflexes in Figure 4.2 in going from the Cu to Cu-Pt product.

Even though Pt appears to protect the Cu, some Cu_2O is still present as shown in Figure 4.2. This may be due to insufficient amounts of Pt being added rendering some Cu particles unprotected. It is also in line with the absence of Pt peaks in the diffractogram, which can be a result of the thinnes of the Pt layer making it difficult for the diffractometer to detect any periodic features. Oxidized forms of Cu may also form in-situ due to incomplete scavenging of ·OH by formate. The resulting byproduct is H_2O_2 which can oxidize Cu before Pt is added. Such a conjecture is supported by the broad absorbance in Figure 4.1a where the Cu plasmon peak is only present as a shoulder, whereas in Figure 4.1d the Cu plasmon peak is more clearly defined. The broadness of the absorbance in Figure 4.1a is thus attributed to the presence of Cu_2O.

The hypothesis of Pt being the protective layer is strongly supported by the electrochemical results. The CV of the Cu-Pt sample in Figure 4.4 exhibits clear signs of Pt being present at the surface as the shape of the voltammogram resembles that of the Pt-sample, which can be seen from the reduction peak matching between the CVs.

It is also supported by the similar behavior during LSV for both the pure Pt and Cu@Pt-samples; the current density normalized with respect to geometric electrode surface area in Figure 4.5a is similar for both samples. When normalizing for the mass of Pt used, the Cu-Pt-sample outperforms the pure Pt-sample as seen in Figure 4.5b. This would not be possible if Pt was not present at the surface, as the pure Cu sample in Figure 4.5a has no activity towards the HER. If the Pt had formed a separate phase, we would expect to see a lower current response in the Cu@Pt-sample due to a much lower Pt surface area as less total Pt was used for this sample. This speaks against the possibility of an alloy having formed; in an alloy Pt would be present in the bulk and we would expect there to be less Pt available at the surface to participate in HER. It also dissuades the notion that some sort of bi/tri-metallic Pt-Cu-Cu_2O nanoparticles have formed, by the same argument. If this was the case we would also expect to see some evidence of oxidation of the Cu phase in Figure 4.4, which we do not.

Even though the XRD, UV-vis and electrochemical results are all consistent with the formation of a core-shell structure, they only show it indirectly. The S(T)EM and EDX maps, however, give a more direct view into the nature of the sample. The dark-field S(T)EM image in Figure 4.3b exhibit clear bright areas which are indicative of heavier elements than the surrounding C material. The EDX maps in Figure 4.3d and 4.3f, which belong to Cu and Pt respectively, overlap to a large degree with these bright spots suggesting that the heavier elements indeed consist of Pt and Cu and that they are present at the same locations. Note that Figure 4.3c, belonging to C, overlaps perfectly with the bright-field S(T)EM image in Figure 4.3a; this is expected because it is the support material onto which the metals are attached. O is also present everywhere, as can be observed in Figure 4.3e, which could indicate metal oxides, but is most likely adsorbed O_2 due to the sample being exposed to air. If the O contribution only came from metal oxides, we would expect more of an overlap with the metals and not with the carbon support.

The catalytic activity found here, an overpotential at -10 mA cm^{-2} of 34.8 mV $\pm$ 14.3 mV, is within the margin of error of a Pt/Ru on vulcan C support reported in [42], which was measured under similar conditions of 0.5 mol dm^{-3} H_2SO_4 electrolyte to be 23 mV. The commercial 20 wt % Pt/C catalyst tested there gave an overpotential of 31 mV at the same conditions. Furthermore, Cao et. al. prepared Pt@Au core-shell nanoparticles on vulcan C support and tested their catalytic activity towards HER, finding it to be 16 mV at -10 mA [43], also finding a performance of 31 mV for their commercial 20 wt % Pt/C reference. These comparisons puts the catalyst tested here on par with a commercial 20 wt % Pt/C catalyst in terms of current density, but in terms of the amount of Pt used ours significantly outperforms it. It also highlights the need for more precise measurements on the Cu@Pt catalyst, as the uncertainty is too large to place it definitively in a good or poorly performing region.

5.1   Sources of error in the experiments

As can be seen in the additional LSV measurements included in Figure B.1, the current response decreases with each measurement made. Even though care was taken to remove any visible gas bubbles on the working electrode between each measurement,

microbubbles of H_2 have most likely formed in the catalyst surface and adsorbed to a significant degree. They cannot easily be removed by mechanical means. Their effect is to reduce the available surface, resulting in the observed decrease in current response for each measurement. One technique to remove them is to do several CVs to oxidize them back to H^+. Further measurements can then be performed without the diminishing effect of the adsorbed microbubbles. Had this been done here, it is possible we would have obtained an even better overpotential at -10 mA cm^{-2} for the Cu-Pt catalyst.

There is some ambiguity in ascribing the emerging shoulder in the UV-vis spectrum in Figure 4.1a to the formation of Cu nanoparticles; although combined with the indirect evidence the conclusion seems valid, direct comparison is made difficult due to the variation in the spectra with particle size and surfactants used. An additional technique to characterize Cu nanoparticles in solution would be desireable.

6   Conclusions and Further Work

Based on the foregoing discussion, all the evidence points towards a successful synthesis of Cu@Pt core-shell nanoparticles. When compared to Pt on porous carbon support, the core-shell catalyst exhibits comparable activity towards HER by surface area and higher activity by unit mass Pt used. The overpotential required to reach -10 mA cm^{-2} was found to be 34.8 mV $\pm$ 14.3 mV. These findings demonstrate that core-shell structured catalysts are useful for reducing the amount of expensive material used while maintaining catalytic activity, and is thus a viable avenue of research to improve the efficacy of hydrogen production in acidic solution by electrolysis.

The results obtained here and some of the conjectures put forth in the discussion provide a fruitful basis for further work. To start with, we attribute the presence of Cu$_2$O in the Cu-Pt synthesis product partially to insufficient amount of Pt being present to cover all Cu particles fully. This hypothesis can be tested by varying the amount of Pt used in the synthesis. If the reduction of Pt occurs mainly due to galvanic displacement, we would expect to see stronger Cu reflexes in the X-ray diffractograms, up to a maximum when all Cu particles are fully covered by Pt. Additional Pt would be reduced sonochemically, possibly forming a separate phase, which would not contribute to the Cu reflexes. Observing such results would then strengthen the conclusions made here.

In the interest of changing the catalytic activity of the outer Pt-shell, repeating a similar synthesis with other core elements would be of great interest; other period IV transition metals would be good candidates. An overview of catalytic activity, for example based on the overpotential to reach -10 mA cm^{-2}, for each element would be an interesting comparison. If a similar behaviour for the reduction of Pt was observed in a UV/vis spectra taken during such syntheses, this would also be in line with our hypothesis of the reduction taking place by galvanic displacement.

In terms of obtaining even more conclusive evidence, higher resolution STEM and EDX images would be highly desirable. Elemental EDX map scans were obtained here, but the resolution was not good enough to obtain EDX line scans over single particles. Such measurements will indicate quite decisively whether a true core-shell structure has been achieved. Furthermore, in regards to more accurate measurements, in section 5.1 we attribute the decreased current response in the LSV measurements in Figure B.1, Appendix A, to the covering of the catalyst surface by bubbles of H$_2$. A way to check if this is indeed the case is to do linear sweeps in both the cathodic and anodic direction; if the obtained curve shows significant signs of hysteresis (anti-symmetry), it is a good indication that this is indeed occurring to the catalyst.

Finally, in terms of realizing practical use of the catalyst made here, two avenues of investigation would be interesting to pursue. The first would be to investigate the performance of the catalyst in realistic conditions; a catalyst is useless in practice if it is not stable over time or easily disrupted by the presence of species other than the electroactive ones. For nanoparticles, stability with time is a major concern as there are strong thermodynamic driving forces towards either particle growth, called Ostwald ripening, or to dissolve back in solution. The second, if the catalyst demonstrates

suitable for practical use, is to investigate how to scale up the synthesis procedure. The work done here only used at most 250 mL liquid volumes; the effect of the volume parameter on the synthesis procedure would be an essential first step to possible commercial applications.

References

[1] Keith Oldham, Jan Myland, and Alan Bond. *Electrochemical science and technology: fundamentals and applications*. John Wiley & Sons, 2011.

[2] John Catillaz Jeffrey Goldmeer. "Hydrogen for power generation whitepaper". In: (2021). URL: https://www.ge.com/gas-power/future-of-energy/hydrogen-fueled-gas-turbines.

[3] Odne Stokke Burheim. *Engineering energy storage*. Academic press, 2017.

[4] Glenk G. and Reichelstein S. "Economics of converting renewable power to hydrogen". In: *Nature Energy* 4 (2019), pp. 216–222. DOI: https://doi.org/10.1038/s41560-019-0326-1.

[5] Bruno G. Pollet, Shyam S. Kocha, and Iain Staffell. "Current status of automotive fuel cells for sustainable transport". In: *Current Opinion in Electrochemistry* 16 (2019). Electrochemical Materials and Engineering • Sensors and Biosensors, pp. 90–95. ISSN: 2451-9103. DOI: https://doi.org/10.1016/j.coelec.2019.04.021.

[6] Manoj B Gawande et al. "Cu and Cu-based nanoparticles: synthesis and applications in catalysis". In: *Chemical reviews* 116.6 (2016), pp. 3722–3811.

[7] A. Sarkar and A. Manthiram. "Synthesis of Pt@Cu CoreShell Nanoparticles by Galvanic Displacement of Cu by Pt4+ Ions and Their Application as Electrocatalysts for Oxygen Reduction Reaction in Fuel Cells". In: *The Journal of Physical Chemistry C* 114.10 (2010), pp. 4725–4732. DOI: 10.1021/jp908933r.

[8] Hong Zhu, Xingwang Li, and Fanghui Wang. "Synthesis and characterization of Cu@Pt/C core-shell structured catalysts for proton exchange membrane fuel cell". In: *International Journal of Hydrogen Energy* 36.15 (2011), pp. 9151–9154. ISSN: 0360-3199. DOI: https://doi.org/10.1016/j.ijhydene.2011.04.224.

[9] ZD Wei et al. "Electrochemically synthesized Cu/Pt core-shell catalysts on a porous carbon electrode for polymer electrolyte membrane fuel cells". In: *Journal of Power Sources* 180.1 (2008), pp. 84–91.

[10] M Neergat and R Rahul. "Unsupported Cu-Pt core-shell nanoparticles: oxygen reduction reaction (ORR) catalyst with better activity and reduced precious metal content". In: *Journal of the Electrochemical Society* 159.7 (2012), F234.

[11] Bruno G Pollet. "The use of ultrasound for the fabrication of fuel cell materials". In: *International Journal of Hydrogen Energy* 35.21 (2010), pp. 11986–12004.

[12] Rachel A. Caruso, Muthupandian Ashokkumar, and Franz Grieser. "Sonochemical formation of colloidal platinum". In: *Colloids and Surfaces A: Physicochemical and Engineering Aspects* 169.1 (2000), pp. 219–225. ISSN: 0927-7757. DOI: https://doi.org/10.1016/S0927-7757(00)00438-6.

[13] Kenji Okitsu et al. "Sonochemical Preparation of Ultrafine Palladium Particles". In: *Chemistry of Materials* 8.2 (1996), pp. 315–317. DOI: 10.1021/cm950285s.

[14] Kenji Okitsu, Muthupandian Ashokkumar, and Franz Grieser. "Sonochemical synthesis of gold nanoparticles: effects of ultrasound frequency". In: *The Journal of Physical Chemistry B* 109.44 (2005), pp. 20673–20675.

[15] Daniel Øvstedal Fakhri. "Sonochemical Synthesis of Pt Nanoparticles on Carbon Support". In: (2021).

[16] Bruno G. Pollet and Muthupandian Ashokkumar. *Introduction to ultrasound, sonochemistry and sonoelectrochemistry*. Springer, Cham, 2019, pp. 2, 4–6. ISBN: 978-3-030-25862-7. DOI: `https://doi.org/10.1007/978-3-030-25862-7`.

[17] Slimane Merouani et al. "Sensitivity of free radicals production in acoustically driven bubble to the ultrasonic frequency and nature of dissolved gases". In: *Ultrasonics sonochemistry* 22 (2015), pp. 41–50. DOI: `https://doi.org/10.1016/j.ultsonch.2014.07.011`.

[18] Mohammad H. Entezari and Peeter Kruus. "Effect of frequency on sonochemical reactions. I: Oxidation of iodide". In: *Ultrasonics Sonochemistry* 1.2 (1994), S75–S79. ISSN: 1350-4177. DOI: `https://doi.org/10.1016/1350-4177(94)90001-9`.

[19] K. Okitsu et al. "Formation of noble metal particles by ultrasonic irradiation". In: *Ultrasonics Sonochemistry* 3.3 (1996), S249–S251. ISSN: 1350-4177. DOI: `https://doi.org/10.1016/S1350-4177(96)00033-8`.

[20] David Armstrong et al. "Standard Electrode Potentials Involving Radicals in Aqueous Solution: Inorganic Radicals". In: *BioInorganic Reaction Mechanisms* 9 (Aug. 2013). DOI: `10.1515/irm-2013-0005`.

[21] Henrik E. Hansen et al. "Two routes for sonochemical synthesis of platinum nanoparticles with narrow size distribution". In: *Mater. Adv.* 2 (6 2021), pp. 1962–1971. DOI: `http://dx.doi.org/10.1039/D0MA00909A`.

[22] H. Scott Fogler. *Elements of Chemical Reaction Engineering*. 4th ed. Pearson Education Limited, 2014. ISBN: 978-1-292-02616-9.

[23] Peter Atkins et al. *Inorganic Chemistry*. 5th ed. Oxford University Press, 2010. ISBN: 978-0-19-923617-6.

[24] Julio de Paula Peter Atkins. *Physical Chemistry*. 10th ed. Oxford University Press, 2014. ISBN: 978-0-19-969740-3.

[25] Vojislav Stamenkovic et al. "Changing the activity of electrocatalysts for oxygen reduction by tuning the surface electronic structure". In: *Angewandte Chemie* 118.18 (2006), pp. 2963–2967.

[26] Alayoglu S. et al. "Ru–Pt core–shell nanoparticles for preferential oxidation of carbon monoxide in hydrogen". In: *Nature Materials* 7 (2008), pp. 333–338. DOI: `https://doi.org/10.1038/nmat2156`.

[27] Ian E. Stewart et al. "Synthesis of Cu–Ag, Cu–Au, and Cu–Pt Core–Shell Nanowires and Their Use in Transparent Conducting Films". In: *Chemistry of Materials* 27.22 (2015), pp. 7788–7794. DOI: `10.1021/acs.chemmater.5b03709`.

[28] Vishal M. Dhavale et al. "Ex-situ dispersion of core–shell nanoparticles of Cu–Pt on an in situ modified carbon surface and their enhanced electrocatalytic activities". In: *Chem. Commun.* 47 (13 2011), pp. 3951–3953. DOI: `10.1039/C0CC05645F`.

[29] Elodie Dalodière et al. "Effect of ultrasonic frequency on H2O2 sonochemical formation rate in aqueous nitric acid solutions in the presence of oxygen". In: *Ultrasonics Sonochemistry* 29 (2016), pp. 198–204. ISSN: 1350-4177. DOI: https://doi.org/10.1016/j.ultsonch.2015.09.014.

[30] Gerold Schwarzenbach, J Muehlebach, and Klaus Mueller. "Peroxo complexes of titanium". In: *Inorganic Chemistry* 9.11 (1970), pp. 2381–2390.

[31] Charles Kittel, Paul McEuen, and Paul McEuen. *Introduction to solid state physics*. Vol. 8. Wiley New York, 2005.

[32] J Alan Creighton and Desmond G Eadon. "Ultraviolet–visible absorption spectra of the colloidal metallic elements". In: *Journal of the Chemical Society, Faraday Transactions* 87.24 (1991), pp. 3881–3891.

[33] I Lisiecki, F Billoudet, and MP Pileni. "Control of the shape and the size of copper metallic particles". In: *The Journal of Physical Chemistry* 100.10 (1996), pp. 4160–4166.

[34] Guglielmo G Condorelli et al. "A single photochemical route for the formation of both copper nanoparticles and patterned nanostructured films". In: *Journal of Materials Chemistry* 13.10 (2003), pp. 2409–2411.

[35] Richard M Crooks et al. "Dendrimer-encapsulated metal nanoparticles: synthesis, characterization, and applications to catalysis". In: *Accounts of chemical research* 34.3 (2001), pp. 181–190.

[36] Takashi Nakamura et al. "Preparation of monodispersed Cu nanoparticles by microwave-assisted alcohol reduction". In: *Bulletin of the Chemical Society of Japan* 80.1 (2007), pp. 224–232.

[37] I Lisiecki and MP Pileni. "Copper metallic particles synthesized" in situ" in reverse micelles: influence of various parameters on the size of the particles". In: *The Journal of Physical Chemistry* 99.14 (1995), pp. 5077–5082.

[38] Anna Maria Raspolli Galletti et al. "Novel microwave-synthesis of Cu nanoparticles in the absence of any stabilizing agent and their antibacterial and antistatic applications". In: *Applied Surface Science* 280 (2013), pp. 610–618.

[39] Yuta Saito et al. "Recent developments concerning the sputter growth of chalcogenide-based layered phase-change materials". In: *Materials Science in Semiconductor Processing* 135 (2021), p. 106079.

[40] Kristin Persson. *Materials Data on Cu (SG:225) by Materials Project*. Apr. 2016. DOI: 10.17188/1204433.

[41] Kristin Persson. *Materials Data on Cu2O (SG:224) by Materials Project*. July 2014. DOI: 10.17188/1207131.

[42] Wei Luo et al. "Boosting HER performance of Pt-based catalysts immobilized on functionalized vulcan carbon by atomic layer deposition". In: *Frontiers in Materials* 6 (2019), p. 251.

[43] Yi Cao et al. "Fe (ii)-Assisted one-pot synthesis of ultra-small core–shell Au–Pt nanoparticles as superior catalysts towards the HER and ORR". In: *Nanoscale* 12.39 (2020), pp. 20456–20466.

Appendices

A   Experimental setup

Pictures of the reactor and its components are given in Figure A.1 below, as well as a demonstration of the full experimental assembly.
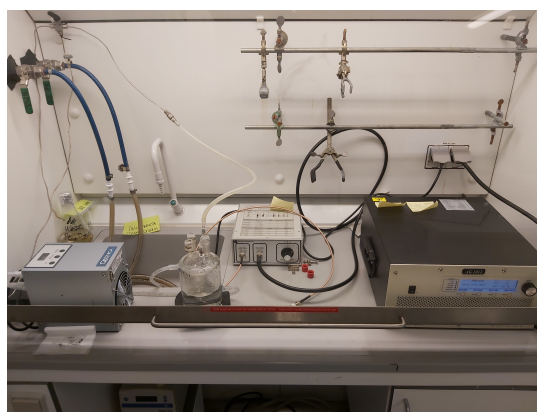

(a)

(b)

(c)

(d)

Figure A.1: Experimental equipment. Plate transducer, silicone ring and plastic holder (a) glass cell and plastic holder (b), and fully assembled sonochemical reactor (c). Finally, an overview of the full experimental setup (d).

B Additional data

Included in Figure B.1 below are all measurement series of linear sweep voltammetry performed on the sonochemically synthesized Cu@Pt on C support. The measurements were performed in order starting with Series 1 followed by 2 and 3. Note the slightly shorter potential region used in Series 1.
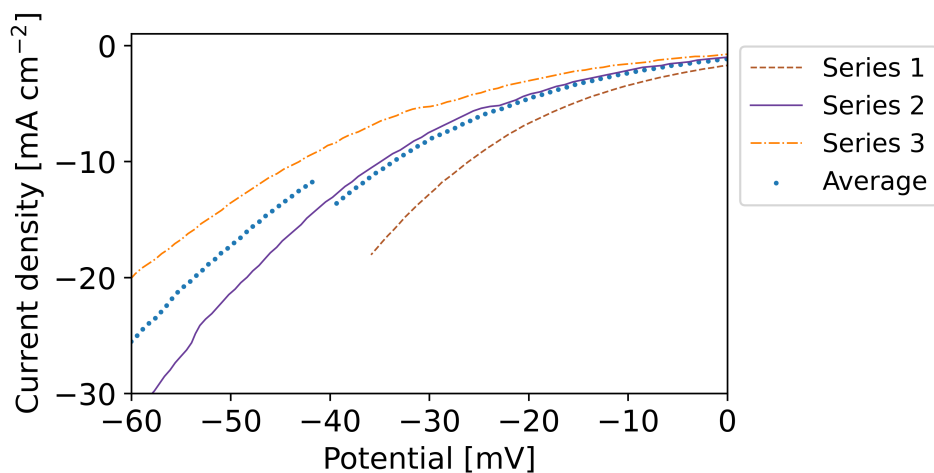
Figure B.1: Linear sweep measurements in the hydrogen evolution region for sonochemically synthesized Cu@Pt on C support. Performed in a 0.5 mol dm^{-3} H$_2$SO$_4$ electrolyte with a RHE. Note the discontinuity in the average curve, as series 1 was done for a shorter potential range than the other two measurements.
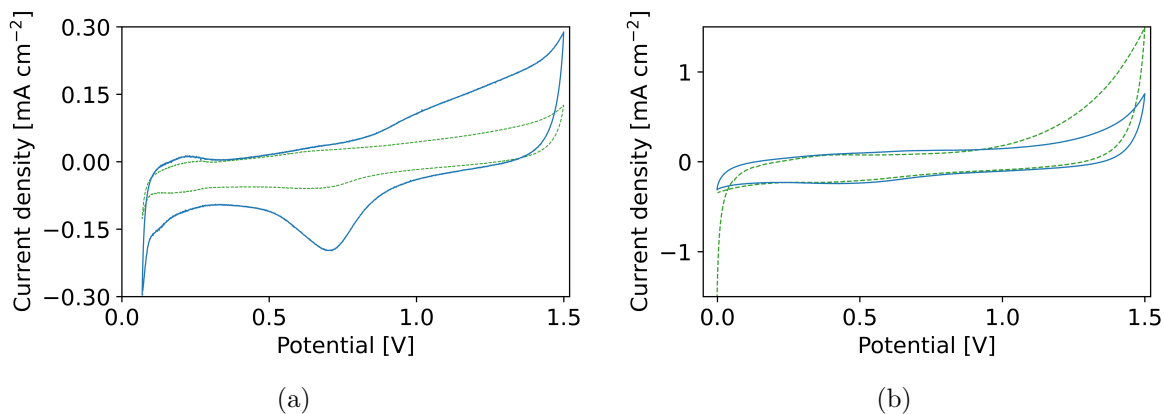
Figure B.2: Additional cyclic voltammograms of (a) the sonochemically synthesized Cu@Pt on C support catalyst and (b) Cu on C support catalyst. In (a), the full line curve is the first cycle and the dashed curve is the last cycle. The same holds for (b)